Journal of Alloys and Compounds 509 (2011) 6859–6863

Contents lists available at ScienceDirect

Journal of Alloys and Compounds

journal homepage: www.elsevier.com/locate/jallcom

Growth of uniform ZnO nanoparticles by a microwave plasma process

T. Wangensteen*, T. Dhakal, M. Merlak, P. Mukherjee, M.H. Phan*, S. Chandra, H. Srikanth, S. Witanachchi*

Department of Physics, University of South Florida, Tampa, FL 33620, United States

ARTICLE INFO

Article history:
Received 20 December 2010
Received in revised form 28 March 2011
Accepted 29 March 2011
Available online 5 April 2011

Keywords:
ZnO nanoparticles
Ferromagnetism
Defects
Plasma

ABSTRACT

ZnO nanoparticle coatings with a controlled size distribution have been grown on quartz substrates by a novel microwave plasma assisted spray (MPAS) technique. This study presents the analysis of structure, photoluminescence, and magnetic properties of particle coatings with two distinctly different mean particle sizes (400 nm and 200 nm). X-ray diffraction patterns show a typical wurtzite structure without any impurity phases for the nanoparticle coatings. SEM and TEM investigations have shown the grown nanoparticles to be spherical and well separated with a narrow size distribution. Nanoparticles are polycrystalline with smaller grain sizes associated with the smaller particle sizes. Photoluminescence (PL) spectra reveal the presence of oxygen vacancy related defects in the 400 nm nanoparticles, which become less pronounced in the 200 nm nanoparticles. The 400 nm nanoparticles are found to exhibit room-temperature ferromagnetism with a clear hysteretic behavior, while the 200 nm nanoparticles are diamagnetic even down to 10 K. These results suggest the oxygen vacancies were the cause for defect-induced ferromagnetism in the 400 nm nanoparticles.

1. Introduction

ZnO is a widely studied material because of its multifunctionality, leading to applications in optoelectronic devices [1], piezoelectricity [2], gas sensing [3], photocatalysis [4], solar cells [5], etc. The direct wide band gap of ZnO (E_g ~3.3 eV at 300 K) with a large exciton binding energy (E_B ~60 meV at 300 K) makes it an excellent material for optoelectronic applications [6]. It has been shown that the optical and electrical properties of ZnO can be tuned by varying growth conditions, introducing dopants, and/or reducing the grain dimensions [7]. These properties can be further manipulated by forming thin films and nanostructures [6–12]. Well separated nanorods of ZnO have been grown and tested for gas sensing due to the increased surface to volume ratio [3]. Nanoparticle coating of ZnO has found applications in electroluminescence [13]. ZnO nanostructures have also been explored in dye-sensitized solar cell (DSSC), which is one of the most promising candidates in photovoltaics [14,15]. Zhang et al. reported a high energy conversion efficiency of up to 5.4% for polydisperse ZnO aggregates based DSSCs [14]. ZnO nanobullets and nanoflakes have recently been studied as active photoanodes in DSSC systems [15]. It has been reported that the light-to-energy conversion efficiency of 3.64% is high for the case of ZnO nanoflakes based DSSCs, while it is 1.93% for the case of nanobullets based DSSCs [15]. From a spintronic application perspective, it is interesting to note that room-temperature ferromagnetism (RTFM) has been reported on undoped and doped ZnO thin films and nanoparticles [16–20]. In this case, a good control over the size distribution of ZnO nanoparticles is vitally important. Until now, synthesis of ZnO nanoparticles has been accomplished by thermal decomposition [21,22], coprecipitation [23,24], combustion [25,26], and sol–gel techniques [8–12,27–32]. In most of these techniques, however, the synthesized nanoparticles are often not spherical and have a large size distribution. An additional high-temperature processing step is also required in order to obtain crystallinity, which may lead to significant side-effects such as the formation of multiple phases [27]. Therefore, development of a new technique for the synthesis of spherical ZnO nanoparticles with a narrow size distribution is of great interest.

In this letter, we report on a novel microwave plasma assisted spray (MPAS) technique for the growth of uniform ZnO nanoparticles. This technique has several advantages over conventional methods, including short reaction time, formed spherical particles, narrow size distribution, and high purity. A comparative study of the magnetic and photoluminescence (PL) properties of 400 nm and 200 nm ZnO nanoparticles are presented.

2. Growth of ZnO nanoparticles

As a first step, molar solutions were prepared by dissolving a stoichiometric amount of zinc acetate $Zn(CH_3COO)_2 \cdot 2H_2O$ in deionized (DI) water. The precursor solution obtained was heated to 60 °C

* Corresponding authors. Tel.: +1 813 974 47 14.
E-mail addresses: twangens@mail.usf.edu (T. Wangensteen), phanm@usf.edu (M.H. Phan), switanach@usf.edu (S. Witanachchi).

0925-8388/$ – see front matter © 2011 Elsevier B.V. All rights reserved.
doi:10.1016/j.jallcom.2011.03.161

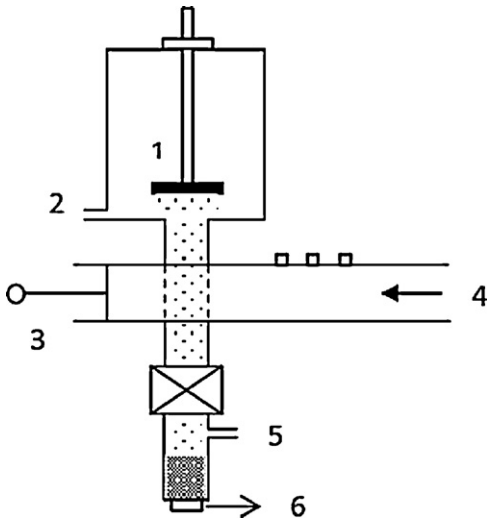

Fig. 1. Schematic of a microwave assisted spray (MAS) system. 1. Substrate. 2. Outlet for vacuum. 3. Microwave waveguide with three tuners and a handle which can slide back and forth to adjust the length of the guide. 4. Microwave input. 5. Inlet for gas flow. 6. Nebulizer below the cylinder which contains the precursor solution.

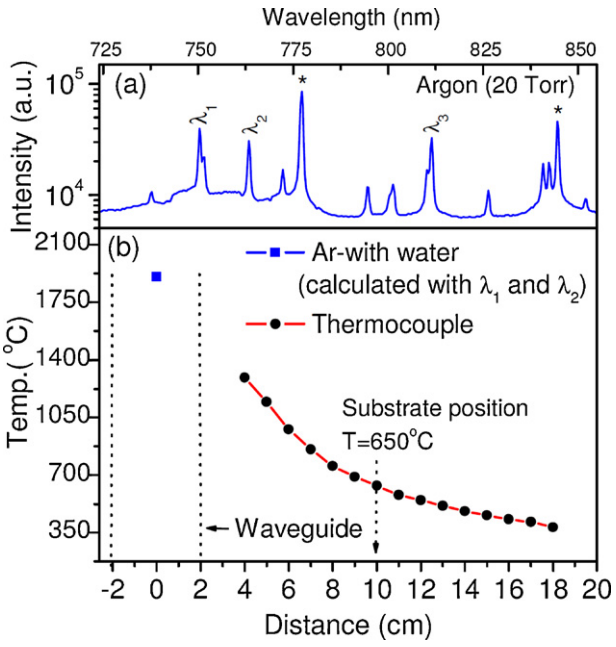

Fig. 2. (a) Spectral lines for argon plasma at 20 Torr. Since it was not reasonable to resolve the sets of three oxygen lines around 777 nm and 844 nm marked by * in the graph, only Ar-lines were used for temperature calculation. (b) Thermocouple measurements made at the operational temperature and pressure of ZnO growth. The location of the waveguide is marked by the vertical lines on the graph. 0 position is the center of the waveguide.

and stirred for 2 h using a magnetic stirrer for uniform dissolution. This solution was used as the precursor in the MPAS process. The precursor solution was transferred into a small cylinder containing an ultrasonic nebulizer on its base. The nebulizer was operated at a frequency of 2.4 MHz to generate uniformly distributed aerosols of the precursor with an average droplet size of 1–1.5 μm. The aerosol from the nebulizer carried by oxygen or argon was injected into a quartz tube which contained the plasma reaction zone (Fig. 1). High temperature plasma of argon gas and water vapor or oxygen was formed within the tube by tuning the waveguides. The chamber was kept at a constant pressure of about 30 Torr in order to maintain a constant rate of spray. As the aerosol droplets pass through the plasma, absorption of microwaves caused water to evaporate reducing the salt to a particle. By controlling the precursor concentration the final size of the salt particle can be controlled [32]. Further heating of the particles in their transit through the plasma led to the completion of the oxidation reaction of Zn to form the oxide. Particles were deposited onto a substrate as they exit the quartz tube into the chamber. One of the main advantages of this process is the completion of the particle formation and chemical reactions in the gas phase, and thus does not rely on the substrate temperature.

One of the important parameters of the plasma for nanoparticle growth is the temperature. Plasma temperatures of close to 2000 °C were measured by spectroscopic methods. The spectroscopic method used to compute temperature is described below. Temperature calculation was performed based on the Boltzmann distribution using the emission line intensities of the plasma (Fig. 2a) at various conditions [33]. The Boltzmann distribution for the emission intensities can be written as

$$\ln\left(\frac{I_{ij}\lambda_{ij}}{g_{ij}A_{ij}}\right) = -\frac{E_i}{kT} + C \quad (1)$$

where I_{ij} is the intensity of the emission line, λ_{ij} is the wavelength of the line corresponding to the energy of transition from i to j, g_i is the known statistical weight or degeneracy of the excited state, A_{ij} is the transition probability of i to j transition, E_i is the excitation energy, k is the Boltzmann constant, T is the absolute temperature and C is a constant.

Thus a plot between $\ln(I_{ij}\lambda_{ij}/g_{ij}A_{ij})$ and the excited energy E_i would be a straight line with a slope of $1/kT$, from which the temperature can be obtained. Since the plasma pressure was relatively high (30 Torr), local thermal equilibrium was expected. Therefore, temperature calculated based on plasma emission would represent the real temperature of the plasma environment. Relative intensity of two well separated spectral lines of the same atomic species were used to calculate the slope. Spectral data were taken along the vertical axis of the quartz tube in the high intensity regime of the plasma. Light from the plasma was collected by an optical fiber that was inserted through an observation hole. Spectra were obtained by feeding the optical output from the fiber into a spectrometer. Fig. 2a shows spectral lines of argon plasma, while water vapor was flowing to the chamber kept at a pressure of 30 Torr. The magnitudes of monatomic argon signature energy peaks were recorded. Temperatures were estimated only using argon spectral lines with and without the flow of water vapor. Argon line pairs were chosen for these measurements at pair one wavelengths of λ_1 = 750.38 nm and λ_2 =763.51 nm; and pair two wavelengths of λ_1 = 750.38 nm and λ_3 = 811.53 nm, respectively. The obtained temperatures were on the order of 2000 °C, and are depicted in Table 1. Oxygen temperature would be even higher, since it has a smaller mass than the argon, and additionally when combined with collisions from H_2O gas, the overall heat transfer would be greater than the argon. The temperature of the plasma past the microwave waveguide, in the direction of the moving gas was measured with a K-type thermocouple. The thermocouple measurements were made at the operational temperature and pressure of ZnO growth and can be seen as solid circles in Fig. 2b. These direct temperature measurements could be done only to within 4 cm from the center of the waveguide without damaging the thermocouple. The tem-

Table 1
Temperatures (T) in °C calculated from two sets of well separated spectral line-pairs of argon plasma using Eq. (1).

	w/o water	w/water	Line pairs (nm)
$T1$	1905	1828	λ_1 = 750.38 and λ_2 = 763.51
$T2$	2043	2051	λ_1 = 750.38 and λ_3 = 811.53

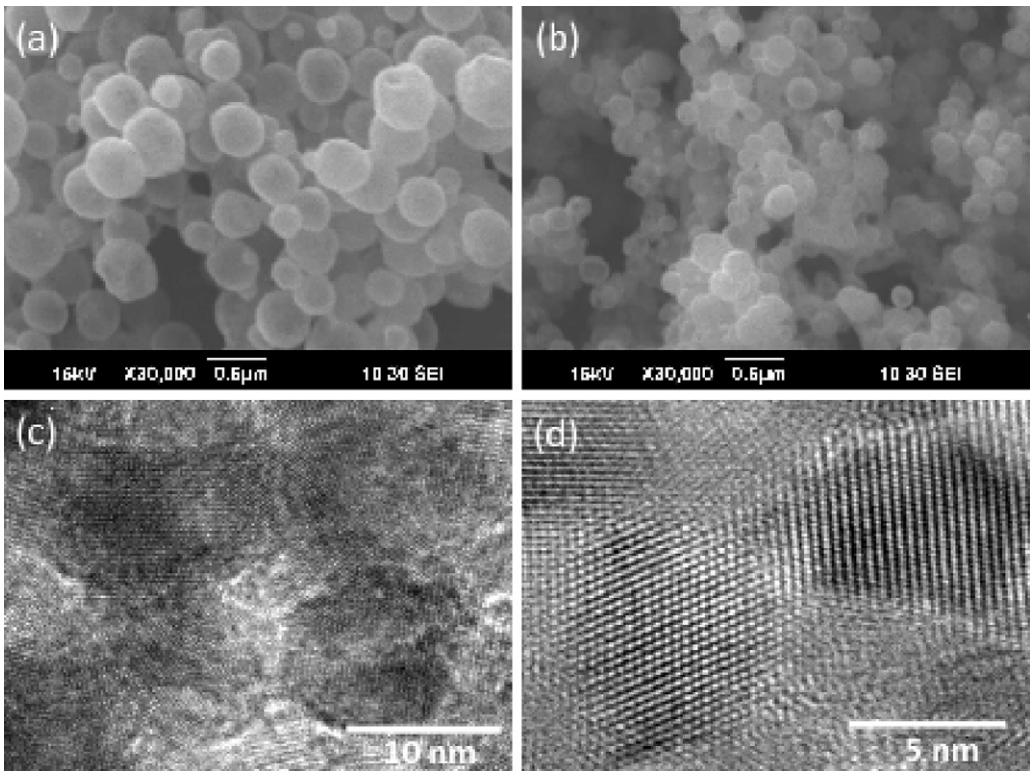

Fig. 3. SEM images of (a) 400 nm and (b) 200 nm ZnO nanoparticles at 30KX magnification. TEM images of (c) 400 nm and (d) 200 nm ZnO nanoparticles.

perature of the plasma at the center of the waveguide (calculated from the spectral lines) would fall on the trend line of the thermocouple temperature data if extrapolated. The temperature data confirmed that the necessary temperature to complete the reaction was reached, and the cooling profile showed that a fairly high temperature was maintained for some time after passing through the waveguide. Furthermore, the presence of high-intensity spectral lines at 775 nm and 846 nm that correspond to atomic oxygen indicate the high reactivity of the plasma in the formation of ZnO. This in combination with the high average plasma temperature allowed the nebulized droplets to fully crystallize before reaching the substrate as confirmed by XRD, SEM, and TEM.

Since the precursor has the necessary components dissolved in solution, the process consisted of several steps. The chemical process began when initial heating caused the evaporation of the solvent, condensing the material within individual droplets to smaller particles. After the solute evaporated, the chemicals that were contained in the droplet reacted with oxygen and formed ZnO nanocrystals before they were deposited onto the substrate. The chemical reactions are summarized as follows [34]:

$$Zn(CH_3COO)_2{\cdot}2H_2O \rightarrow Zn(CH_3COO)_2 + 2H_2O \quad (2)$$

$$Zn(CH_3COO)_2 + 4O_2 \rightarrow ZnO + 3H_2O + 4CO_2 \quad (3)$$

The solvent, (water in this case) evaporated first. Then, as shown in reaction (2), the dihydrates evaporated from the remaining droplet. Next, as the droplets passed through the center of the plasma, the acetates broke their bonds from the Zn, and the free Zn combined with oxygen to make ZnO particles as depicted in reaction (3). The airborne particles completed all reactions during transit and were then deposited on silicon substrates. The substrate, which was placed at 10 cm away from the center of the waveguide, was heated (T = 650 °C) by the plasma heat to enhance the adhesion of the nanoparticles onto the substrate.

3. Results and discussion

3.1. Structural analysis

The structure, morphology and crystallinity of the nanoparticle samples have been studied by X-ray diffraction (XRD), scanning electron microscopy (SEM), and transmission electron microscopy (TEM). Fig. 3 shows the SEM and TEM photographs of the nanoparticles at two different concentrations of precursor solution (0.25 M and 0.03125 M, respectively). It can be observed that the nanoparticles are spherical and well separated, with a narrow size distribution for both concentrations. The average diameter of each particle varies from 400 nm for 0.25 M to 200 nm for 0.03125 M. Within each individual nanoparticle exists a number of small crystallities. High resolution TEM (HRTEM) images (Fig. 3c and d) reveal the presence of larger crystallites (average size around 12 nm) in each 400 nm particle, as compared to those of each 200 nm particle (average size around 6 nm). The crystallinity of the 200 nm nanoparticles is better than that of the 400 nm nanoparticles. It is worth mentioning that the crystallite size scales with the particle size, which can be tuned by varying the concentration of the precursor solution used.

Fig. 4 shows the XRD patterns of bulk ZnO (obtained from Alfa Aesar with 99.99% purity) and the 400 nm and 200 nm nanoparticle samples. It can be seen that like in the case of bulk ZnO, the ZnO nanoparticles possess a characteristic hexagonal lattice with space group $P63mc$(186). No impurity peaks were observed even in the logarithmic scale. In addition, no amorphous peak was detected in the XRD scan.

3.2. Magnetic and photoluminescence properties

The magnetic properties of the ZnO nanoparticle samples have been studied using a commercial Physical Property Measurement System (PPMS) from Quantum Design with a temperature range of

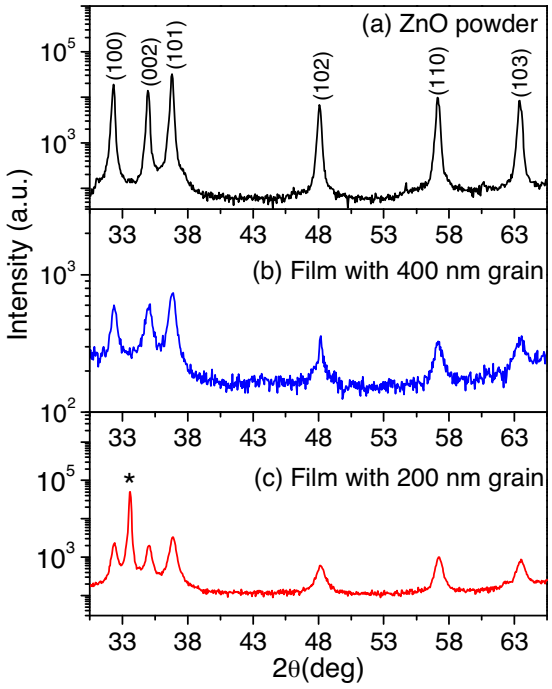

Fig. 4. XRD patterns of (a) bulk ZnO, (b) 400 nm and (c) 200 nm ZnO nanoparticles grown on Si (1 0 0) substrate. (*) is the peak due to the silicon substrate. Miller Indices for these peaks are (1 0 0): 33, (0 0 2): 36, (1 0 1): 37, (1 0 2): 48, (1 1 0): 57, (1 0 3): 63.

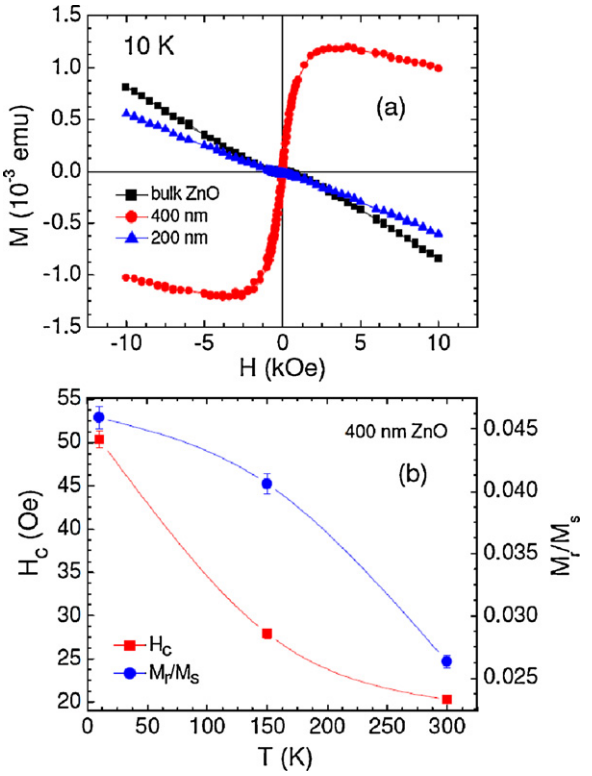

Fig. 5. (a) M–H curves of bulk, 400 nm and 200 ZnO nanoparticles; (b) temperature dependence of coercivity (H_c) and the remanent to saturation magnetization ratio (M_r/M_s) extracted from the M–H curves for the 400 nm ZnO nanoparticles.

5–300 K and applied fields up to 7 T. The M–H data were recorded at 10 K, 150 K, and 300 K for the 400 nm and 200 nm nanoparticles. The M–H data of bulk ZnO are also included for comparison. Interestingly, we find that the 400 nm nanoparticles are ferromagnetic at 300 K, while the bulk and 200 nm nanoparticles are diamagnetic even down to 10 K. Fig. 5a shows the M–H loops taken at 10 K for these three samples. The values of coercive field (H_c) and the remanent to saturation magnetization ratio (M_r/M_s) extracted from the M–H loops of the 400 nm nanoparticles are plotted against temperature (T), as shown in Fig. 5b. It can be observed that the H_c and M_r/M_s significantly decrease with increasing temperature. The H_c decreases from ~50 Oe at 10 K to ~20 Oe at 300 K. This trend suggests the intrinsic ferromagnetism of the 400 nm ZnO nanoparticles. The saturation magnetization of the 400 nm ZnO nanoparticles at 300 K is $M_S \sim 0.0074$ emu/g, which is comparable to that of the 9 nm ZnO nanoparticles reported by Inamdar et al. ($M_S \sim 0.008$ emu/g) [21].

One of the questions posed by this research is the reason for room-temperature ferromagnetism observed in the 400 nm nanoparticles but not in the 200 nm nanoparticles. We recall that the RTFM has been observed in undoped and doped ZnO nanoparticles [18,19,21,25,27]. Sundaresan et al. [27] argued that the origin of RTFM in undoped ZnO nanoparticles could be the exchange interactions between localized electron spin moments resulting from oxygen vacancies at the surfaces of the nanoparticles. Garcia et al. [18] showed the possibility of inducing RTFM in ZnO nanoparticles without doping with magnetic transition metal ions (Co or Mn) but simply alternating the surface electronic configuration of the nanoparticles by capping them with organic molecules. Magnetization and Raman spectra studies on ZnO nanoparticles annealed in air at different temperatures ranging from 450 °C to 800 °C revealed that the RTFM decreased as the annealing temperature increased [23]. These results point to the importance of oxygen vacancies in inducing RTFM in undoped ZnO nanoparticles. However, Zhang and Xie have recently argued that for ZnO nanoparticles annealed in air at high temperatures (600 °C, 800 °C, and 1000 °C) the RTFM is attributed to the oxygen vacancy related defects, but for ZnO nanoparticles annealed in air at lower temperatures (e.g. 400 °C) the RTFM arises mainly from the interstitial Zn defects [28]. Recent theoretical calculations have also suggested that both oxygen and zinc vacancies can induce RTFM into ZnO [35]. In fact both Zn interstitials and oxygen vacancies donate two electrons, leading to the difficulty in distinguishing one from the other using electrical measurements [36].

In order to address this issue in the present case, we have studied the photoluminescence (PL) spectra of both the 400 nm and 200 nm ZnO nanoparticles. PL has proved useful for investigating the defects that are present in ZnO [8–12,21,28,36,37]. In the present study, a HeCd laser (325 nm) was used as an excitation source and carriers were excited to emit PL spectra. Fig. 6 shows the PL spectra of the 400 nm and 200 nm ZnO nanoparticles. As one can see clearly in this figure, for both samples the ultraviolet (UV) emission is observed at 387 nm, which corresponds to a band gap of 3.203 eV. A broad green emission with a major peak at around 542 nm is observed for the 400 nm nanoparticles, but this feature is largely suppressed in the 200 nm nanoparticles. The peaks at 663 nm, which are particle size independent, are due to the HeCd gas discharge plasma. It has been suggested that the green emission (around 542 nm) results from the recombination of electrons with holes trapped in singly ionized oxygen vacancies [21,28,37]. The intensity of the green emission can be used to quantitatively evaluate the oxygen vacancy concentration in ZnO. It has been shown that the increase of the oxygen vacancy concentration leads to the increase of the intensity of the green emission [28,37]. This clearly suggests, in our case, that more oxygen vacancies are present in the 400 nm ZnO nanoparticles than in the 200 nm ZnO nanoparticles. This can be reconciled with the fact that the crystallinity of the 200 nm nanoparticles is better than that of the 400 nm nanoparticles, as confirmed by HRTEM (Fig. 3c and d), and

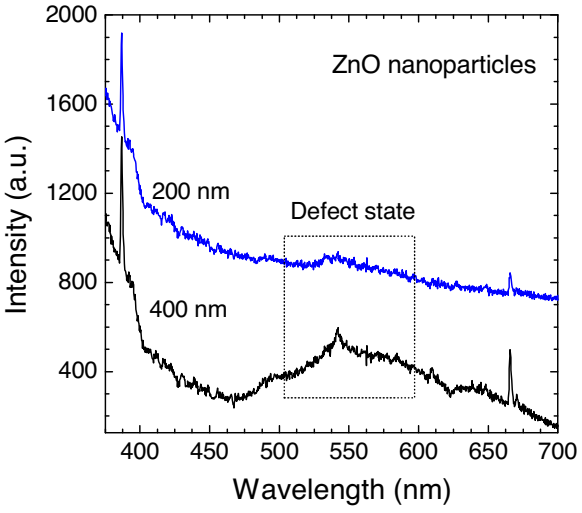

Fig. 6. Room temperature PL spectra of the 400 nm and 200 nm ZnO nanoparticles. Defect related green emission is observed for the 400 nm ZnO nanoparticles.

XRD. The reason for poor crystallinity in 400 nm particles in comparison to that of 200 nm particles can be explained as follows. For the two concentrations that were considered here, the multiple of two in radius corresponds to a factor of 8 differences in volume. This nearly an order of magnitude difference in material volume in the same reaction environment causes the oxidation of Zn in the smaller particle to be more complete leading to stoichiometric ZnO. Additionally, ZnO particles formed at the high temperature plasma zone goes through a rapid quenching process as they exit the plasma. This gives rise to higher density of grain boundaries in the larger particle which accounts for the high density of defects. In connection with the M–H data, it is logical to infer that the oxygen vacancy related defects are sufficient to induce the ferromagnetism in the 400 nm nanoparticles but not in the 200 nm nanoparticles. This result is consistent with the previous observation [37] that annealing ZnO nanoparticles in oxygen atmosphere reduced the number of oxygen vacancies, leading to a suppression of the PL peak related to the green emission and hence the ferromagnetism in the material.

4. Conclusions

A novel microwave plasma assisted spray technique has been developed that allows growth of spherical ZnO nanoparticles with a narrow size distribution in a single step. In this technique, the size of the nanoparticles is dependent on the concentration of the precursor used. Each nanoparticle consists of multiple nanocrystallites, and the size of the crystallites within each particle scales with the particle size. The oxygen vacancy related defects that are observed in ZnO nanoparticles (400 nm) with large crystallites (12 nm), become much less pronounced in ZnO nanoparticles (200 nm) with small crystallites (6 nm). The room-temperature ferromagnetism observed in the larger ZnO nanoparticles (400 nm) arises mainly from the oxygen vacancy related defects, which correlated with defects also seen in PL spectra. A more complete study to determine the onset of ferromagnetism as a function of the size (defect incorporation) would be very interesting future work. The ZnO nanoparticles grown by this technique are also desirable for gas sensing or a host material of a solar cell sensitizer as the surface to volume ratio is the highest for spherical particles.

Acknowledgements

The authors would like to thank Dino Ferizovic, Lindsay Hussey, and Dr. Martin Munoz for their assistance with obtaining the spectral data. This work was partially supported by the Department of Defense under the grant W81XWH-07-1-0708. HS and MHP acknowledge support from DoE-BES through Grant no. DE-FG02-07ER46438.

References

[1] R.D. Vispute, V. Talyansky, S. Choopun, R.P. Sharma, T. Venkatesan, M. He, X. Tang, J.B. Halpern, M.G. Spencer, Y.X. Li, L.G. Salamanca-Riba, A.A. Iliadis, K.A. Jones, Appl. Phys. Lett. 73 (1998) 348.
[2] A.D. Corso, M. Posternak, Raffaele, A. Baldereschi, Phys. Rev. B 50 (1994) 10175.
[3] Q.H. Li, T. Gao, Y.G. Wang, T.H. Wang, Appl. Phys. Lett. 86 (2005) 123117.
[4] M. Dutta, D. Basak, Nanotechnology 20 (2009) 475602.
[5] G. Hua, Y. Zhang, J. Zhang, X. Cao, W. Xu, L. Zhang, Mater. Lett. 62 (2008) 4109.
[6] A.B. Djurisic, A.M.C. Ng, X.Y. Chen, Prog. Quant. Electron. 34 (2010) 191.
[7] Ü. Özgür, Ya.I. Alivov, C. Liu, A. Teke, M.A. Reshchikov, S. Doğan, V. Avrutin, S.-J. Cho, H. Morkoç, J. Appl. Phys. 98 (2005) 041301.
[8] R. Yousefi, B. Kamaluddin, Solid State Sci. 12 (2010) 252.
[9] R. Yousefi, B. Kamaluddin, J. Alloys Compd. 479 (2009) L11.
[10] R. Yousefi, M.R. Muhamad, J. Solid State Chem. 183 (2010) 1733.
[11] R. Yousefi, B. Kamaluddin, Appl. Surf. Sci. 255 (2009) 9376.
[12] A. Zhang, J. Tan, H. Huang, S. Chen, M. Wang, S. Xu, Appl. Surf. Sci. 257 (2011) 4051.
[13] C.Y. Lee, Y.T. Haung, W.F. Su, C.F. Lin, Appl. Phys. Lett. 89 (2006) 231116.
[14] Q. Zhang, T.P. Chou, B. Russo, S.A. Jenekhe, G. Cao, Adv. Funct. Mater. 18 (2008) 1654.
[15] J. Mou, W. Zhang, J. Fan, H. Deng, W. Chen, J. Alloys Compd. 509 (2011) 961.
[16] P. Sharma, A. Gupta, K.V. Rao, F.J. Owens, R. Sharma, R. Ahuja, J.M. Osorio Guillen, B. Johansson, G.A. Gehring, Nat. Mater. 2 (2003) 673.
[17] N.H. Hong, J. Sakai, V. Brize, J. Phys.: Condens. Matter. 19 (2007) 036219.
[18] M.A. Garcia, J.M. Merino, E. Fernandez Pinel, A. Quesada, J. de la Venta, M.L. Ruız Gonzalez, G.R. Castro, P. Crespo, J. Llopis, J.M. Gonzalez-Calbet, A. Hernando, Nano Lett. 7 (2007) 1489.
[19] Z.H. Zhang, X.F. Wang, J.B. Xu, S. Muller, C. Ronning, Q. Li, Nat. Nanotechnol. 4 (2009) 523.
[20] D. Mukherjee, T. Dhakal, H. Srikanth, P. Mukherjee, S. Witanachchi, Phys. Rev. B 81 (2010) 205202.
[21] D.Y. Inamdar, A.D. Lad, A.K. Pathak, I. Dubenko, N. Ali, S. Mahamuni, J. Phys. Chem. C 114 (2010) 1451.
[22] M.S. Niasaria, F. Davara, A. Khansari, J. Alloys Compd. 509 (2011) 61.
[23] D.Q. Gao, Z.H. Zhang, J.L. Fu, Y. Xu, J. Qi, D.H. Xue, J. Appl. Phys. 105 (2009) 113928.
[24] R. Chauhan, A. Kumar, R.P. Chaudhary, J. Optoelectron. Biomed. Mater. 3 (2011) 17.
[25] G.Q. Pei, C.T. Xia, F. Wu, J. Xu, J. Alloys Compd. 467 (2009) 539.
[26] M.L. Dinesha, H.S. Jayanna, S. Mohanty, S. Ravi, J. Alloys Compd. 490 (2010) 618.
[27] A. Sundaresan, R. Bhargavi, N. Rangarajan, U. Siddesh, C.N.R. Rao, Phys. Rev. B 74 (2006) 161306.
[28] Y.Z. Zhang, E. Xie, Appl. Phys. A 99 (2010) 955.
[29] A.K. Zak, M.E. Abrishami, W.H.Abd. Majid, R. Yousefi, S.M. Hosseini, Ceram. Int. 37 (2011) 393–398.
[30] A.K. Zak, W.H.Abd. Majid, M.E. Abrishami, R. Yousefi, Solid State Sci. 13 (2011) 251–256.
[31] A.K. Zak, W.H.Abd. Majid, M. Darroudi, R. Yousefi, Mater. Lett. 65 (2011) 70–73.
[32] G. Dedigamuwa, Masters' Thesis, University of South Florida, 2005.
[33] S. Semenov, B. Cetegen, J. Therm. Spray Technol. 10 (2001) 326.
[34] S.H. Yang, C.Y. Lu, J. Electrochem. Soc. 154 (2007) J397.
[35] X. Zuo, S.D. Yoon, A. Yang, W.H. Duan, C. Vittoria, V.G. Harris, J. Appl. Phys. 105 (2009) 07C508.
[36] L. Schmidt-Mende, J.L. MacManus-Driscoll, Mater. Today 10 (2007) 40.
[37] Q.T. Pan, K. Huang, S. Ni, F. Yang, S. Lin, D. He, J. Phys. D: Appl. Phys. 40 (2007) 6829.